

Learning-Based Modeling of a Magnetically Steerable Soft Suction Device for Endoscopic Endonasal Interventions

Majid Roshanfar^{a,*}, Alex Zhang^b, Changyan He^c, Amir Hooshidar^d, Dale J. Podolsky^a, Thomas Looi^a, Eric Diller^{b,e}

^a*The Wilfred and Joyce Posluns Centre for Image Guided Innovation & Therapeutic Intervention (PCIGITI), The Hospital for Sick Children (SickKids), Toronto, ON, Canada*

^b*Department of Mechanical and Industrial Engineering (MIE), University of Toronto, Toronto, ON, Canada*

^c*School of Engineering, University of Newcastle, Newcastle, NSW, Australia*

^d*Surgical Performance Enhancement and Robotics (SuPER) Centre, Department of Surgery, McGill University, Montreal, QC, Canada*

^e*Institute of Biomedical Engineering (BME), University of Toronto, Toronto, ON, Canada*

Abstract

This paper introduces a novel learning-based modeling framework for a magnetically steerable soft suction device designed for endoscopic endonasal brain tumor resection. The device is miniaturized (4 mm outer diameter, 2 mm inner diameter, 40 mm length), 3D printed using biocompatible SIL 30 material, and integrates embedded Fiber Bragg Grating (FBG) sensors for real-time shape feedback. Shape reconstruction is represented using four Bezier control points, allowing for a compact and smooth representation of the device's deformation. A data-driven model was trained on 5,097 experimental samples covering a range of magnetic field magnitudes (0–14 mT), actuation frequencies (0.2–1.0 Hz), and vertical tip distances from the surface of the electromagnet coil table (90–100 mm), using both Neural Network (NN) and Random Forest (RF) architectures. The RF model outperformed the NN across all metrics, achieving a mean root mean square error of 0.087 mm in control point prediction and a mean shape reconstruction error of 0.064 mm. Feature importance analysis further revealed that magnetic field components predominantly influence distal control points, while frequency and distance affect the base configuration. This learning-based approach effectively models the complex nonlinear behavior of hyperelastic soft robots under magnetic actuation without relying on simplified physical assumptions. By enabling sub-millimeter shape prediction accuracy and real-time inference, this work represents an advancement toward the intelligent control of magnetically actuated soft robotic tools in minimally invasive neurosurgery.

Keywords: Soft robotics, magnetic actuation, shape sensing, Fiber Bragg Grating (FBG), endoscopic neurosurgery, continuum robots, data-driven modeling.

1. Introduction

An endoscopic endonasal approach is a well-established, minimally invasive alternative to traditional craniotomy, aimed at reducing trauma to the brain and surrounding critical neurovascular structures [1]. By making use of natural anatomical pathways through the nasal cavity, this technique eliminates the need for large scalp incisions or bone removal, reducing patient complications and recovery time [2]. It involves removing a portion of the sinus cavity using a surgical drill to create a narrow surgical corridor for the insertion of two primary instruments: an endoscopic camera for high-definition visualization and a surgical tool, typically a suction or cutting device, for tissue manipulation. Together, these instruments enable surgeons to operate within deep and confined spaces, performing precise dissection and controlled, stepwise removal of tumor tissue under continuous visual guidance (see Fig. 1). Clinical studies have demonstrated that this approach offers favorable neurological outcomes, shorter hospital stays, and reduced postoperative

complications, particularly in pediatric patients with intracranial and skull base tumors [3, 4].

However, the effectiveness of the endoscopic endonasal approach is often constrained by patient-specific anatomical complexities, such as a reduced skull base, narrow nasal passages, and underdeveloped sphenoid sinuses [5]. These anatomical challenges significantly restrict the maneuverability of conventional rigid and straight instruments, increasing the risk of unintentional damage to critical structures like blood vessels, optic nerves, and the brainstem. As a result, surgical precision, safety, and access to certain tumor locations can be compromised. To address these limitations, flexible robotic instruments have been introduced [6], leveraging the compliance and adaptability of their materials to navigate complex and curved anatomical pathways [7, 8]. These systems aim to minimize tissue trauma while enhancing dexterity, reach, and control within confined surgical environments. Nevertheless, the inherent nonlinear and elastic behavior of flexible robotic instruments, combined with the lack of intuitive control and real-time shape feedback, continues to pose significant challenges for safe and effective clinical use.

With these challenges in mind, magnetic actuation has also

*Corresponding author.

Email address: majid.roshanfar@sickkids.ca (Majid Roshanfar)

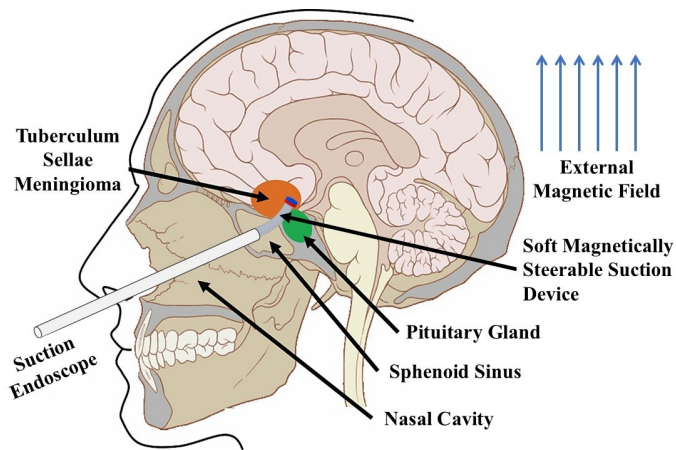


Figure 1: Magnetically steerable soft suction device for endoscopic endonasal brain tumor resection. The device is introduced through the nasal cavity and sphenoid sinus using a conventional suction endoscope to access deep-seated regions at the skull base. A hollow cylindrical permanent magnet at the tip of the soft robot enables remote steering via externally applied magnetic fields. This magnetic actuation allows the device to navigate around critical anatomical structures, such as the pituitary gland, to precisely target and extract tumor tissue (e.g., tuberculum sellae meningioma).

emerged as a transformative solution for enhancing the control and flexibility of medical devices and robotic systems in minimally invasive procedures [9, 10, 11]. By applying external magnetic fields, forces and torques can be wirelessly transmitted to the distal end of instruments [12, 13], eliminating bulky mechanical linkages, cables, or fluidic systems. This approach reduces mechanical complexity, avoids issues like friction and backlash, and enables precise, remote control of devices within the body. Magnetic actuation has been successfully employed in medical applications such as catheter steering [14], microsurgical tools [15], endoscopy [16], targeted drug delivery [17], and microbiome sampling [18], among others. Typically, magnetically controlled robots are constructed either by attaching permanent magnets to the distal tip to create steerable catheters [19], or by embedding ferromagnetic particles within soft elastomers, such as PDMS or thermoplastic polyurethane, to fabricate flexible, continuum robots capable of controlled deformation [20]. These designs allow safe navigation through intricate anatomical structures, improving surgical access, reducing patient trauma, and offering enhanced maneuverability [21, 22].

Recognizing the potential of combining soft robotics and magnetic actuation, a prior study in [23] demonstrated the feasibility of integrating a magnetically steerable soft tip with a conventional rigid suction device to overcome the limitations of straight, rigid tools in endoscopic procedures. The prototype in the previous study featured soft segments made from Ecoflex 00-50 embedded with a permanent magnet, and it achieved controlled in-plane bending angles exceeding 90° under moderate magnetic fields (below 25 mT). The device was fabricated using mold-based casting techniques, offering both sufficient suction capability and flexibility. Validation experiments in simulated neurosurgical environments, using agar-based brain phantoms,

demonstrated that the device could safely access target sites and perform precise tumor extraction, highlighting its potential to improve the safety and efficacy of minimally invasive neurosurgical interventions.

While the feasibility of the device has been previously studied, it relied on a simplified mechanical model based on constant curvature (CC) kinematics and an equivalent Young’s modulus to predict bending behavior [23]. Although this approach provided reasonable accuracy for basic teleoperation, it was limited in its ability to fully capture the complex, nonlinear, and hyperelastic behavior of soft materials under varying magnetic fields and loading conditions. The CC assumption neglected strain-dependent stiffening, axial forces, shear effects, and dynamic interactions, particularly during large deformations or when subjected to non-uniform magnetic fields. Also, the fabrication process, based on mold-casting with non-biocompatible materials, constrained scalability, miniaturization, and clinical translation. To overcome these limitations (as summarized in the Table 1, this study introduces a novel magnetically steerable soft suction device designed specifically for endoscopic endonasal brain tumor resection, featuring a miniaturized, biocompatible structure fabricated via direct 3D printing. The device integrates embedded fiber Bragg grating (FBG) sensors to enable real-time shape sensing.

Shape estimation in flexible robots can generally be achieved using either sensor-free or sensor-based methods. Sensor-free approaches rely on kinematic or magnetic models to infer shape without embedded sensors [28, 24], while sensor-based techniques use embedded elements for direct measurement [25, 26]. Our method follows the sensor-based approach, combining FBG data with a learning-based model to enable accurate, real-time shape prediction. More importantly, a learning-based modeling framework is proposed to replace the traditional mechanical models. This data-driven approach directly maps magnetic field inputs to the device’s shape using Bezier curve control points, effectively capturing the nonlinear deformation behavior without relying on oversimplified physical assumptions on the magnetic field actuation and robotic dynamics. This enables precise shape prediction, improved control, and adaptability across diverse surgical scenarios. To the best of our knowledge, this is the first magnetically actuated soft suction device equipped with a learning-based shape prediction model tailored for neurosurgical applications. The key contributions are:

- Design and fabrication of a miniaturized, 3D-printed magnetically steerable soft suction device using biocompatible material, with integrated FBG sensors for real-time shape sensing,
- Development of a data-driven modeling framework that directly maps magnetic field inputs to device shape using a Bezier curve representation,
- Experimental validation demonstrating high shape prediction accuracy across a range of magnetic field strengths and actuation frequencies, effectively addressing the nonlinear behavior of hyperelastic materials.

Table 1: Comparison of Analytical and Learning-Based Modeling Approaches in Soft Robotics.

Study	Application	Approach	Advantages	Limitations
Kim [20]	Magnetic soft robots	Analytical	Magnetic continuum modeling	Static behavior only
Roshanfar [24]	Hybrid soft robot	Analytical	Models hyperelastic stiffening	Not adaptive to dynamic inputs
Masoumi [25]	Force sensing	Learning	Handles nonlinearities	Sensor-specific
Torkaman [26]	6-DoF sensing	Learning	Compact, embedded sensing	Hardware-specific model
Pittiglio [16]	Magnetic catheter	Analytical	Autonomous, personalized motion	Requires imaging and maps
He [13]	Neurosurgical tools	Analytical	Precise magnetic tip control	Rigid design; complex planning
Dreyfus [14]	Endovascular robot	Analytical	High dexterity for vascular paths	No deformation modeling
Hooshiar [27]	Tip force estimation	Analytical	Sensor-free; physics-based	Requires exact motion input
Jolaei [28]	Sensor-free control	Analytical	Lightweight contact model	Limited soft behavior accuracy
Sayadi [29]	Shape prediction	Analytical	Extended piecewise constant curvature	Requires segmentation
This work	Magnetic soft robot	Learning	Real-time, accurate and robust	Needs experimental dataset

2. Materials and Methods

2.1. Shape Encoding

Accurate shape reconstruction is essential for controlling flexible, magnetically actuated soft robots. In this work, shape sensing is achieved using a multi-core fiber (MCF) embedded with fiber Bragg gratings (FBG), combined with a Bezier curve-based representation to provide a compact and smooth model of the device's deformation. This approach not only reduces high-dimensional sensor data into a small set of control points but also ensures smoothness and continuity in the reconstructed shape. The resulting representation is well-suited for integration into learning-based models, enabling both efficient training and real-time inference.

2.1.1. FBG-Based Shape Sensing with Multi-Core Fiber

The soft suction device was integrated with an MCF containing 26 FBGs uniformly spaced at 10 mm intervals along a sensing length of 250 mm. The MCF is an off-the-shelf shape-sensing sensor purchased from FBGS company (FBGS, Belgium). The outer diameter (OD) of the FBG fiber was 0.38 mm, allowing seamless embedding within the inner channel of the soft robot. FBGs function by reflecting a specific wavelength of light, known as the Bragg wavelength (λ_B), which shifts in response to axial strain ($\Delta\varepsilon$) and temperature variations (ΔT). This shift is governed by [30]:

$$\frac{\Delta\lambda_B}{\lambda_{B0}} = S_\varepsilon\Delta\varepsilon + S_T\Delta T \quad (1)$$

where λ_{B0} is the initial Bragg wavelength, S_ε and S_T are sensitivity coefficients for strain and temperature, respectively. In the symmetric MCF configuration, the central core serves for temperature compensation, while the outer cores measure bending-induced strain. The strain in each outer core is:

$$\Delta\varepsilon_i = \frac{\Delta\lambda_{B,i}}{S_\varepsilon\lambda_{B0,i}} - \frac{\Delta\lambda_{B,1}}{S_\varepsilon\lambda_{B0,1}} \quad (2)$$

then, the curvature (κ) and bending angle (θ_b) at each grating location are derived using [30]:

$$\kappa = \frac{2\|\kappa_{\text{app}}\|}{N}, \quad \theta_b = \angle\kappa_{\text{app}} \quad (3)$$

where:

$$\kappa_{\text{app}} = -\sum_{i=1}^N \frac{\varepsilon_i}{r} \cos(\theta_i) \hat{\mathbf{i}} - \sum_{i=1}^N \frac{\varepsilon_i}{r} \sin(\theta_i) \hat{\mathbf{j}} \quad (4)$$

and:

$$\varepsilon_i = -\kappa r \sin\left(\theta_b - \frac{3\pi}{2} - \theta_i\right) \quad (5)$$

where r is the radial distance from the center to the outer cores (one central core with three evenly spaced radial cores), $N = 3$ is the number of outer cores, and θ_i is the angular position of each core. The curvature vector κ_{app} denotes the apparent bending curvature at each segment, expressed as a 2D vector in the plane orthogonal to the fiber axis. Its magnitude represents the bending curvature, while its angle defines the bending plane direction θ_b . Note that this formulation assumes planar bending between FBG nodes and does not account for geodesic curvature or torsion.

Next, the MCF embedded within the soft robot was connected to an optical interrogator (FBGS, Belgium), which continuously monitored wavelength shifts in each of the 26 FBGs. These wavelength shifts, induced by bending-related strain, were sampled in real-time (30 Hz) and transmitted to a processing unit via a transmission control protocol (TCP) connection established with a custom MATLAB script. For each grating, the interrogator provided axial strain values from the outer cores of the MCF. Using Eq. 2, temperature-compensated strain $\Delta\varepsilon_i$ was calculated by referencing the central core, which is insensitive to bending. The resulting strain values were then converted into local curvature (κ) and bending plane angle (θ_b) for each grating position, following the geometric relationship defined in Eq. 5.

Once the curvature and curvature bending angle profiles were obtained, the MATLAB script reconstructed the 3D shape of the soft robot's centerline by applying a piecewise constant curvature (PCC) approach between each grating. The total sensing length was discretized into 25 uniform segments, each corresponding to the interval between adjacent FBGs with a fixed arc length of 10 mm. For each segment, if the curvature κ was close to zero, it was treated as a straight section with a pure translation along the local axial direction. When curvature was

present, the segment was modeled as a circular arc, where the radius was defined as $r = 1/\kappa$ and the bending angle θ was computed as $\kappa \cdot ds$. A local rotation matrix was constructed for each segment to align the bending direction according to θ_b , and the corresponding transformation was applied. These local transformations, consisting of rotation and translation, were sequentially propagated along the length of the fiber to build the global shape.

To mitigate numerical drift accumulated through successive matrix multiplications, singular value decomposition (SVD) was applied at each step to maintain orthogonality of the rotation matrices. The 3D Cartesian coordinates of the robot's centerline were extracted from the origins of the cumulative transformation matrices, resulting in a set of 26 points representing the reconstructed backbone. Finally, the total arc length of the reconstructed shape was computed to ensure that the final shape accurately matched the known physical length of 250 mm. This reconstruction process effectively converts raw optical strain data into a precise 3D representation of the soft robot's shape. By leveraging the PCC assumption, the algorithm achieves a balance between computational efficiency and sufficient accuracy for real-time surgical navigation. The reconstructed centerline serves as the basis for fitting a Bezier curve, providing a compact and smooth representation suitable for integration into the learning-based control framework.

2.1.2. Bezier Curve Representation of the Soft Robot Shape

Flexible continuum robots, such as the magnetically actuated soft suction device in this study, naturally exhibit smooth and continuous deformation patterns. These characteristics make them ideal candidates for representation using spline-based methods. Among various spline families, Bezier curves are widely adopted due to their mathematical simplicity, ability to generate smooth curves, and intuitive geometric control through a limited number of points [27, 29]. A cubic Bezier curve, in particular, offers the minimal degree necessary to approximate constant-curvature shapes, which are common in soft robotic and catheter-like structures. In this study, a cubic Bezier curve was employed to approximate the shape of the soft robot reconstructed from discrete FBG sensor data. The Bezier curve defines a continuous path, parameterized by $s \in [0, 1]$, using four control points \mathbf{p}_0 , \mathbf{p}_1 , \mathbf{p}_2 , and \mathbf{p}_3 , as:

$$\mathbf{c}(s) = (1-s)^3\mathbf{p}_0 + 3s(1-s)^2\mathbf{p}_1 + 3s^2(1-s)\mathbf{p}_2 + s^3\mathbf{p}_3 \quad (6)$$

where, $\mathbf{c}(s)$ represents the position vector along the curve at any normalized parameter $s \in [0, 1]$, where $s = 0$ indicates the base of the curve (\mathbf{p}_0) and $s = 1$ indicates the tip of the curve (\mathbf{p}_3). The first and last control points, \mathbf{p}_0 and \mathbf{p}_3 , are constrained to coincide exactly with the base and tip points of the FBG-reconstructed centerline, ensuring that the Bezier curve satisfies the physical boundary conditions of the soft robot in each frame. The intermediate control points, \mathbf{p}_1 and \mathbf{p}_2 , govern the curvature profile and the smooth transition along the curve. An important modeling assumption is that the total length of the soft robot remains constant during magnetic actuation. This constraint ensures that the Bezier curve fitting adheres to the

physical behavior of the device without introducing artificial elongation or compression. The role of \mathbf{p}_1 and \mathbf{p}_2 extends beyond simple geometric placement. As highlighted in [27], the positioning of these control points directly influences the curvature characteristics of the Bezier curve. A shape parameter λ can be introduced to conceptually control the convexity of the curve. While in this study \mathbf{p}_1 and \mathbf{p}_2 were determined through a least-squares fitting process, understanding the influence of λ provides valuable insight into how control point spacing affects bending behavior. Smaller values of λ correspond to tighter curvature, while larger values result in smoother, more gradual bends.

Using a Bezier curve to represent the shape offers substantial advantages over directly handling the full set of FBG-derived points. Reducing the description from 26 discrete points to just four control points significantly lowers the dimensionality of the data. This compact representation facilitates faster processing, reduces memory requirements, and is particularly advantageous in learning-based models where lower-dimensional outputs improve training efficiency and real-time inference. Furthermore, Bezier curves inherently provide smooth and continuous approximations, which effectively filter out noise present in sensor data, yielding a clearer and more reliable representation of the robot's deformation. The fitting process was formulated as a least-squares optimization problem, aiming to minimize the cumulative Euclidean distance between the continuous Bezier curve $\mathbf{c}(s)$ and the discrete centerline points obtained from FBG reconstruction. Since the number of data points exceeds the number of parameters to estimate, this creates an overdetermined system. The Moore–Penrose pseudoinverse was used to compute the unique solution that minimizes the total squared error, ensuring a stable and balanced fit even in the presence of sensor noise or minor inconsistencies in the data. Let $\mathbf{c}(s_i) \in \mathbb{R}^3$ denote the reconstructed centerline points at normalized arc-length parameters $s_i \in [0, 1]$. Since the endpoints \mathbf{p}_0 and \mathbf{p}_3 are fixed to match the FBG base and tip positions, the problem reduces to solving for the intermediate control points \mathbf{p}_1 and \mathbf{p}_2 that minimize the fitting error:

$$\min_{\mathbf{p}_1, \mathbf{p}_2} \sum_{i=1}^N \left\| \mathbf{c}(s_i) - \mathbf{Q}(s_i) \begin{bmatrix} \mathbf{p}_1 \\ \mathbf{p}_2 \end{bmatrix} \right\|^2 \quad (7)$$

where $\mathbf{Q}(s_i) \in \mathbb{R}^{3 \times 6}$ is the Bezier basis matrix for \mathbf{p}_1 and \mathbf{p}_2 at s_i . Then, the optimal solution is:

$$\begin{bmatrix} \mathbf{p}_1 \\ \mathbf{p}_2 \end{bmatrix} = (\mathbf{Q}^T \mathbf{Q})^\dagger \mathbf{Q}^T \mathbf{C} \quad (8)$$

where $\mathbf{C} = [\mathbf{c}(s_1)^T, \dots, \mathbf{c}(s_N)^T]^T \in \mathbb{R}^{3N}$ is the stacked vector of FBG-derived centerline coordinates. By leveraging fundamental properties of Bezier curves, such as $\mathbf{c}(0) = \mathbf{p}_0$ and $\mathbf{c}(1) = \mathbf{p}_3$, the method inherently satisfies positional boundary conditions. The arc-length constraint is enforced during post-processing by scaling the fitted curve to match the known physical length of the device. Figure 2 illustrates a representative experimental example (for the case of 1 Hz rotation and a 90 mm distance between the tip and the coil table surface) of

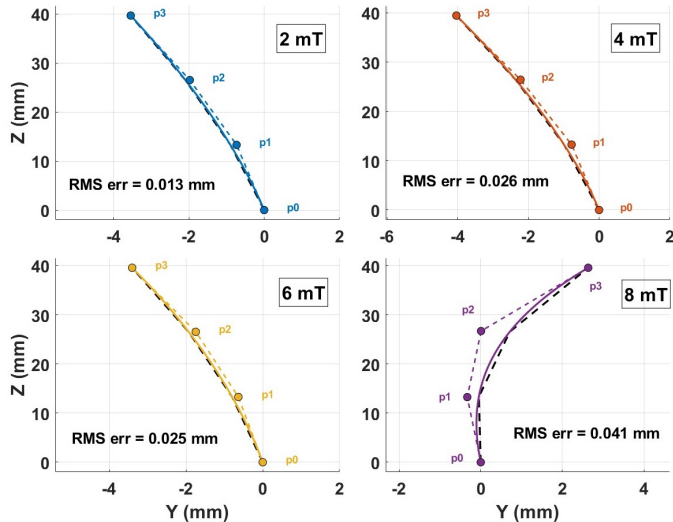


Figure 2: FBG-reconstructed shapes (black dashed lines) and corresponding Bezier curve fits (colored solid lines) for four representative frames during 1.0 Hz magnetic field rotation with the soft robot tip positioned 90 mm above the coil table.

the FBG-reconstructed shape alongside the fitted Bezier curve and its control points. The fitting RMSE between the FBG-reconstructed shapes and the corresponding Bezier curves is also reported for these representative cases. This confirms that Bezier curves provide a computationally efficient, compact, and accurate representation of soft robot deformation, making them highly suitable for integration into the learning-based modeling framework proposed in this study.

3. Experimental Setup

The experimental setup was designed to evaluate the deformation behavior of the soft robot under controlled magnetic fields while capturing real-time shape data through embedded FBG sensors. The soft suction device was fabricated using bio-compatible SIL 30 material (Carbon Inc., Redwood City, California, USA) via digital light synthesis (DLS) 3D printing, ensuring precise geometry and material consistency suitable for medical applications. SIL 30 is a silicone urethane elastomer with a nominal Shore A hardness of 35 (instant), as reported by the manufacturer [31]. The device measured 40 mm in length, with an OD of 4 mm and an inner channel diameter of 2 mm. A hollow cylindrical neodymium permanent magnet (Grade N50, 6.35 mm OD \times 3.18 mm ID \times 3.18 mm thickness, nickel-coated) was securely affixed to the distal tip of the device to enable magnetic steering. The magnet features through-thickness magnetization as shown in Fig. 3, optimized for effective actuation within rotating magnetic fields.

The FBG fiber was threaded through the suction channel to enable continuous shape sensing along the length of the soft robot. The proximal end of the fiber was fixed at the base, while the distal end was anchored at the robot’s tip to ensure consistent alignment and accurate strain transfer during deformation. Owing to the fiber’s small OD (0.38 mm), its integration within the lumen imposed negligible mechanical constraint on the flexibility and natural deformation of the soft robot. The proximal

end of the MCF was clamped onto a linear actuator, which allowed fine control over the vertical positioning of the soft robot relative to the electromagnetic coil system’s surface. Both the soft robot and the linear actuator were mounted onto a custom-designed aluminum frame to maintain structural stability and ensure consistent experimental conditions throughout data collection. Additionally, two 3D-printed supports were employed to secure both the base of the FBG fiber and the soft robot to the linear actuator, minimizing unwanted vibrations or displacement. For visual monitoring, two Logitech cameras were positioned orthogonally, providing multi-angle views of the robot’s deformation during actuation.

Magnetic actuation was achieved using an electromagnetic navigation system comprising eight high-power coils arranged beneath the workspace [32]. This system was engineered to deliver spatially controllable magnetic fields while maximizing workspace accessibility. The coil system was capable of generating magnetic fields up to 38 mT along the x and y axes, and up to 47 mT along the z axis at a working height of 120 mm above the coil surface. During each experimental run, an in-plane rotating magnetic field was applied parallel to the xy plane to induce controlled bending and rotation of the robot’s tip (Fig. 4). The applied magnetic field vector followed a sinusoidal form given by:

$$\mathbf{b}(t) = A[-\sin(\omega t), \cos(\omega t), 0]^T \quad (9)$$

where A is the magnetic field magnitude (ranging from 0 to 14 mT) and $\omega = 2\pi f$ is the angular frequency corresponding to the rotation frequency f (0.2, 0.4, 0.6, 0.8, and 1 Hz). This dynamic formulation generated a uniform circular magnetic field in the xy plane, producing a time-varying torque on the embedded tip magnet that resulted in cyclic bending motion. As shown in Fig. 4, the blue and red curves represent the b_x and b_y components, respectively, generating a circular rotating field in the XY plane. To illustrate the magnetic field conditions applied during soft robot actuation, we visualized the in-plane rotating magnetic field components (b_x, b_y) for the 0.2 Hz excitation frequency across magnetic field magnitudes from 2 mT to 14 mT ($b_z = 0$). These sinusoidal field profiles correspond directly to the workspace visualizations presented in Fig. 5, where tip deformation was analyzed under identical field conditions.

A dynamic field was deliberately applied to capture the frequency dependent deformation characteristics of the soft robot, which are influenced by the viscoelastic behavior of the silicone material. As shown in Figs. 6, the same magnetic field magnitude led to larger rotation radii at higher frequencies, highlighting the presence of dynamic effects. The chosen frequency range (0.2–1 Hz) was selected to reflect typical motion speeds observed during endoscopic procedures, ensuring the evaluation remained within clinically relevant operational conditions. To record the data, the robot’s tip was initially positioned 100 mm above the electromagnetic coil table surface. Upon completion of the test series at this height, the linear actuator was used to adjust the tip position to 90 mm above the table surface, and the full set of experiments was repeated under identical conditions to assess the influence of vertical distance on soft robot performance. These two heights were selected to represent clin-

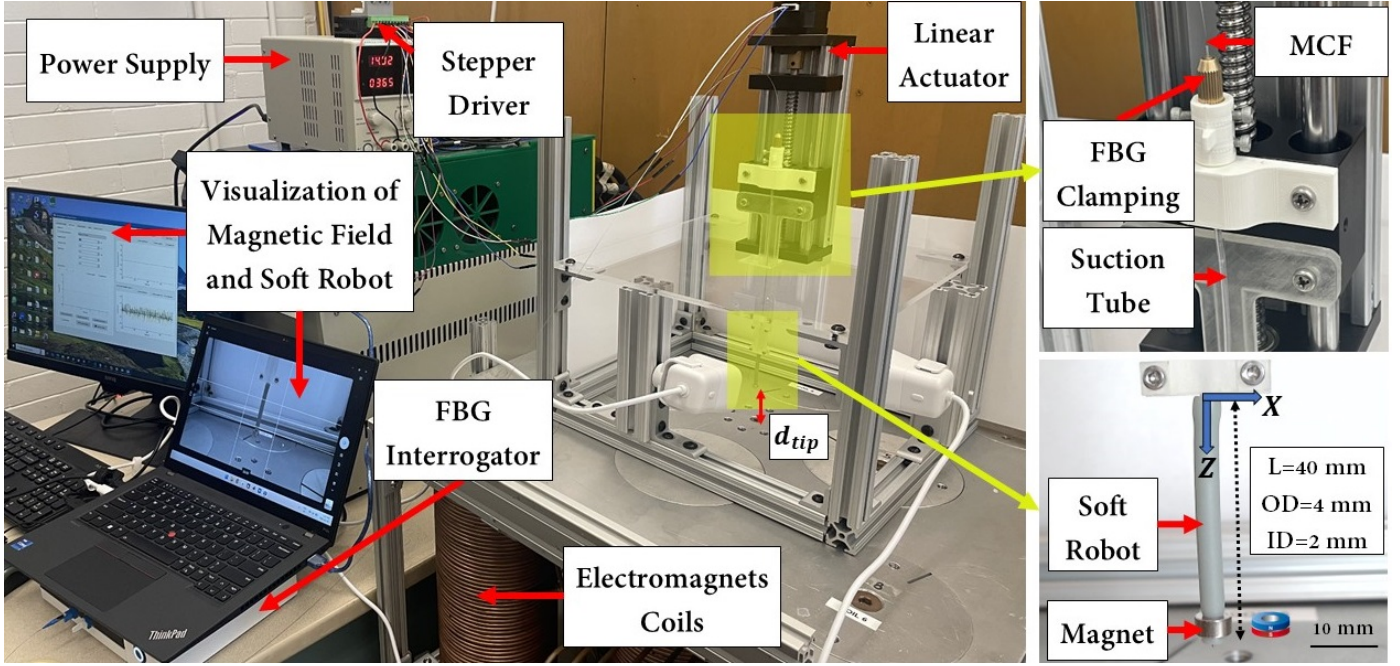


Figure 3: Experimental setup for magnetic actuation and shape sensing of soft robot. The system includes an FBG-embedded soft robot mounted on a linear actuator, positioned above electromagnetic coils at a distance of d_{tip} . A power supply and stepper driver control the linear actuation, while real-time strain data is collected via the FBG interrogator and visualized on a workstation. Close-ups on the right show the FBG clamping, suction tube, 3D printed fixtures, and the soft robot with a tip magnet for steering.

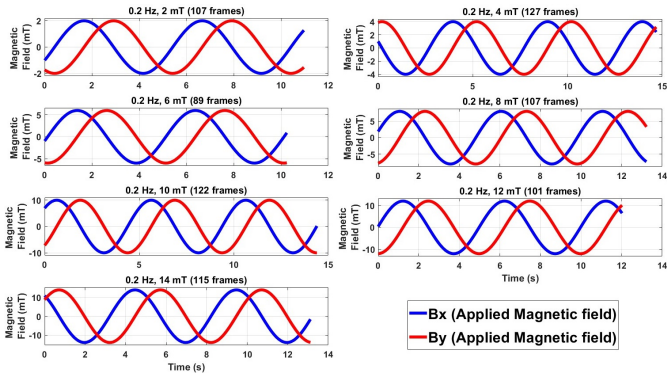


Figure 4: Time-varying magnetic field components (b_x, b_y) for the 0.2 Hz trials corresponding to the trajectories in Fig. 5.

ically relevant working distances that fall within the safe operating range of the electromagnetic coil system, while ensuring measurable differences in magnetic field strength and resulting deformation. In total, 70 distinct actuation scenarios were conducted, covering all combinations of magnetic field strengths, rotation frequencies, and the two vertical distances. Throughout these tests, the strain data from all 26 FBG gratings were continuously recorded at a sampling rate of 30 Hz using a custom MATLAB script interfaced via TCP with the optical interrogator. Following data acquisition, the recorded 250 mm sensing length of the MCF was processed in post-experiment analysis. Only the final 40 mm segment, which corresponds precisely to the embedded length within the soft robot, was retained for shape reconstruction and modeling.

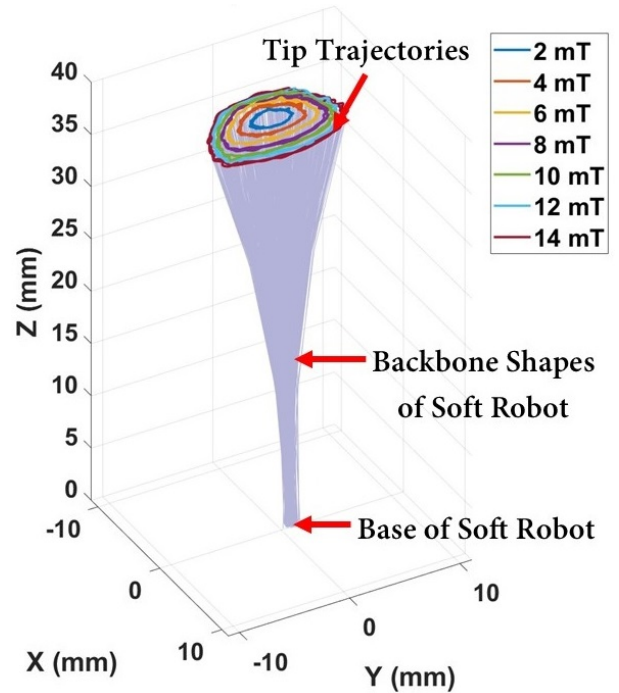


Figure 5: 3D shape reconstruction (0.2 Hz). Each curve represents a centerline shape reconstructed from FBG data at different magnetic field strengths.

4. EVALUATIONS AND DISCUSSION

This section presents a comprehensive evaluation of the learning based approaches used for modeling the soft suction de-

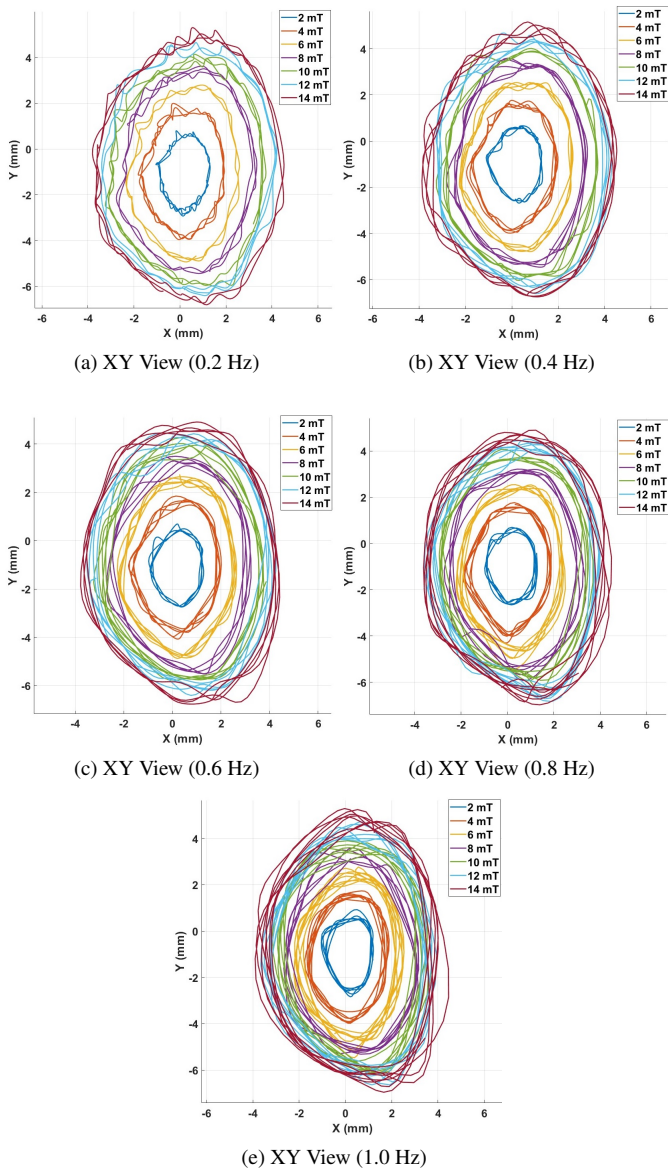


Figure 6: XY-view trajectories at five actuation frequencies. Each panel shows tip paths reconstructed from FBG data under varying magnetic field strengths.

vice. We compare the performance of Neural Network (NN) and Random Forest (RF) models in predicting Bezier control points from magnetic field parameters, analyze feature importance, and evaluate shape reconstruction accuracy in the following sections.

4.1. Dataset Characteristics and Model Training

The dataset consists of 5,097 samples representing various device configurations under different magnetic field conditions. We randomly split the data into training (80%) and testing (20%) sets. The input features include b_x , b_y , magnetic field magnitude, actuation frequency, and tip distance from the coil system. For the NN model, we implemented a feedforward architecture with three hidden layers (64, 32, and 16 neurons) using the Levenberg-Marquardt backpropagation algorithm. As shown

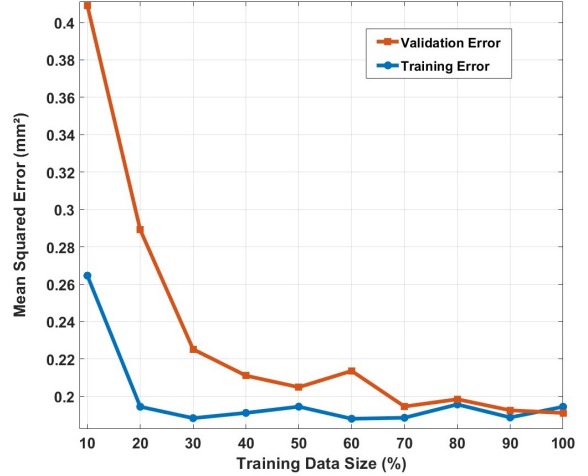


Figure 7: Neural Network learning curve analysis showing the relationship between training data size and model performance.

in Fig. 7, the model achieved optimal performance at approximately 30% of the training data, with minimal improvement thereafter, suggesting efficient learning from a relatively small portion of the dataset. The overall correlation coefficient across all 12 output variables was $R = 0.90574$. For the RF model, we trained 12 separate regressors using 200 trees per forest with a minimum leaf size of 5.

4.2. Model Performance Comparison

Table 2 presents the detailed performance metrics of both models across all control points. The RF model outperforms the NN model, achieving an overall 28.37% reduction in RMSE. This improvement is particularly pronounced for the distal control points (\mathbf{p}_2 and \mathbf{p}_3), which are critical for accurate device tip positioning. The model accuracy comparison by individual control points, as shown in Figs. 8 and 9, reveals that while both models predict proximal control points (\mathbf{p}_0 and \mathbf{p}_1) with similar accuracy, the RF model outperforms the NN model for distal control points (\mathbf{p}_2 and \mathbf{p}_3). Quantitatively, the RF model reduces RMSE by 5.97% for \mathbf{p}_0 , 5.47% for \mathbf{p}_1 , 16.41% for \mathbf{p}_2 , and an impressive 53.94% for \mathbf{p}_3 compared to the NN model. The error distribution analysis reveals that both models exhibit primarily zero-centered errors (Fig. 10), with the RF model demonstrating tighter error distributions across all control points. The NN model struggles with \mathbf{p}_3 coordinates, exhibiting error exceeding 1.5 mm for p_{3Y} , while the RF model maintains max absolute errors below 1.11 mm.

4.3. Feature Importance Analysis

To gain insights into the relationship between magnetic field parameters and device deformation, we analyzed the feature importance metrics derived from the RF model. Our results revealed distinct patterns of influence across different control points: The magnetic field components (b_x and b_y) dominate the influence on most control point coordinates, with b_y showing particularly high importance (>50%) for p_{0Y} , p_{2Y} , and p_{3Y} coordinates. This aligns with the physical understanding of

Table 2: Performance comparison between Neural Network (NN) and Random Forest (RF) models.

Points	Neural Network			Random Forest		
	RMSE (mm)	R ² -	Max Error (mm)	RMSE (mm)	R ² -	Max Error (mm)
p_{0X}	0.088	0.761	0.376	0.083	0.790	0.340
p_{0Y}	0.157	0.428	0.698	0.148	0.493	0.743
p_{0Z}	0.009	0.503	0.049	0.008	0.563	0.044
p_{1X}	0.098	0.811	0.413	0.094	0.828	0.395
p_{1Y}	0.167	0.461	0.803	0.157	0.524	0.869
p_{1Z}	0.010	0.612	0.061	0.010	0.648	0.060
p_{2X}	0.115	0.973	0.393	0.096	0.981	0.362
p_{2Y}	0.180	0.971	0.903	0.152	0.979	0.917
p_{2Z}	0.015	0.979	0.061	0.011	0.989	0.050
p_{3X}	0.227	0.986	0.946	0.095	0.998	0.415
p_{3Y}	0.336	0.990	1.562	0.162	0.998	1.110
p_{3Z}	0.052	0.985	0.236	0.026	0.996	0.125
Overall	0.121	0.788	1.562	0.087	0.816	1.110

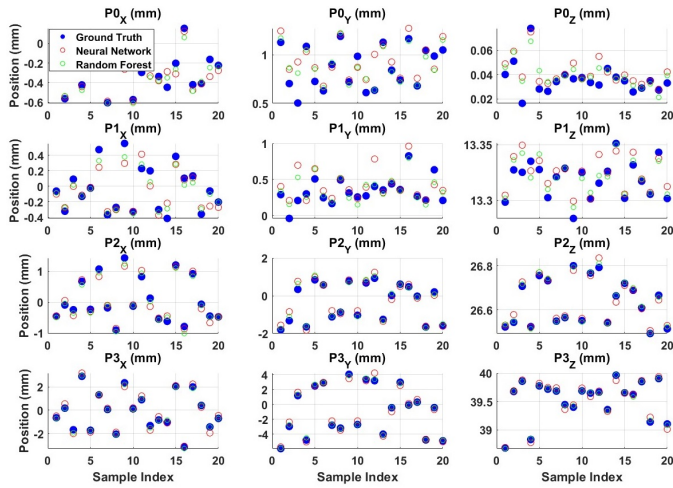


Figure 8: Prediction accuracy for all Bezier control points. Blue dots: ground truth, red circles: NN predictions, green circles: RF predictions.

magnetic actuation, where the Y-component of the magnetic field primarily controls lateral movement of the device. The frequency parameter exhibits uniquely high importance (32.34%) for p_{0Z} , suggesting that actuation frequency plays a significant role in determining the base height of the device. The distance parameter shows consistent influence on \mathbf{p}_0 coordinates (23.81% for p_{0X} , 24.50% for p_{0Z}) and \mathbf{p}_3 coordinates (13.00% for p_{3X} , 13.17% for p_{3Y} , 15.79% for p_{3Z}), reflecting how the proximity to the electromagnetic coil system affects both the fixed base and the free tip of the device. This feature importance analysis provides valuable insights for control system design, indicating which magnetic field parameters should be prioritized for precise manipulation of specific device coordinates. For instance, fine control of the device tip position would ben-

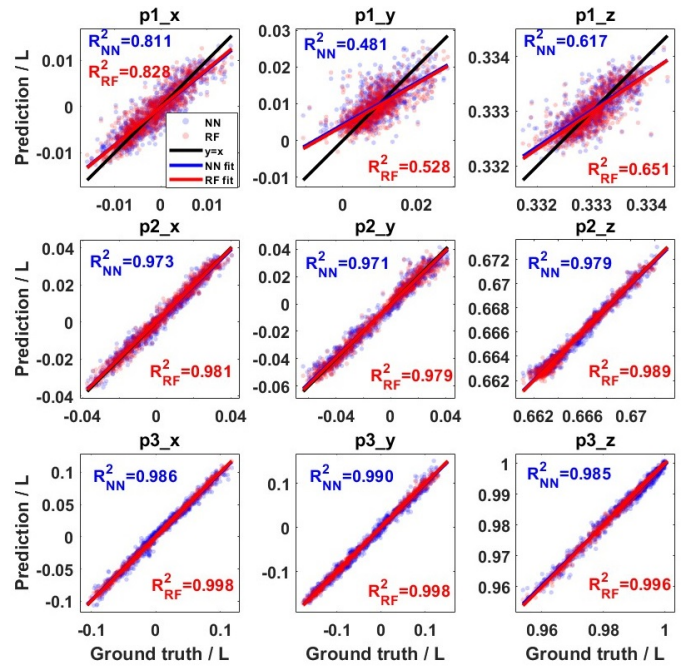


Figure 9: Comparison of NN-predicted and actual Bezier control points across training, validation, testing, and full datasets.

efit from careful modulation of both b_x and b_y , while actuation frequency could be leveraged for height adjustment at the device base.

4.4. Bezier Curve Shape Reconstruction

Beyond individual control point accuracy, we evaluated the overall shape reconstruction performance by comparing the Bezier curves generated from predicted control points with ground truth curves. Figures 11 and 12 illustrate this comparison for both

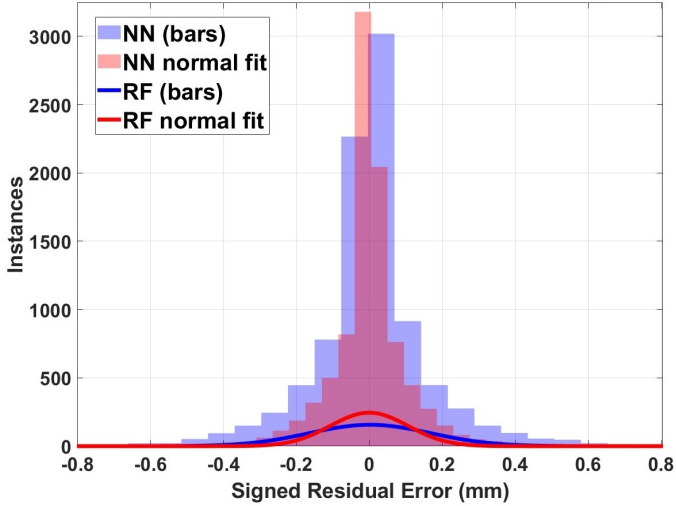


Figure 10: Error histogram showing the distribution of prediction errors. The concentration of errors around zero indicates unbiased predictions.

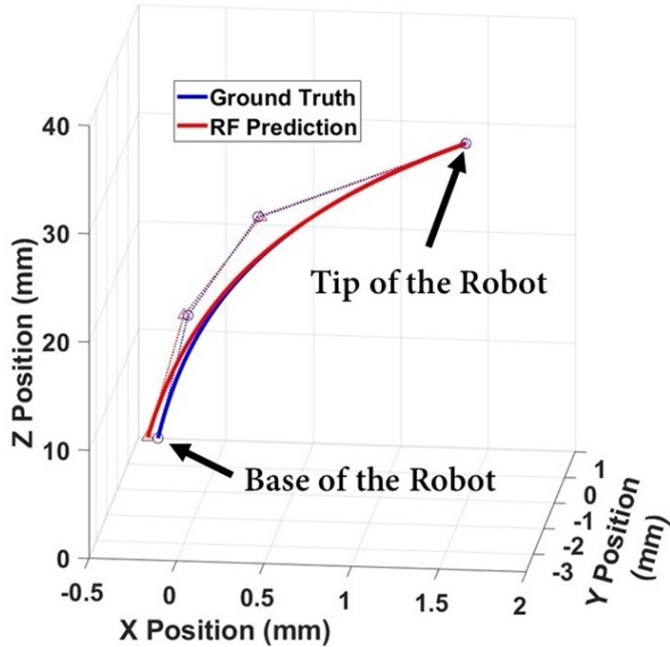


Figure 11: Bezier curve shape prediction (3D view). Ground truth (blue) vs. RF predictions (green).

3D and top-view perspectives. The 3D visualization confirms that the RF model achieves excellent shape reconstruction across diverse deformation patterns. Predicted Bezier curves follow the ground-truth trajectories closely, preserving control-point placement and smooth interpolation. Quantitatively, the RF delivers a MAE of 0.064 mm and a 95th-percentile error of 0.225 mm, both negligible relative to the device diameter (4 mm) and therefore suitable for safe navigation around delicate skull-base anatomy during endoscopic endonasal procedures.

The regression analysis of the NN model (Fig. 9) yielded correlation coefficients of $R_{\text{train}} = 0.9169$, $R_{\text{val}} = 0.8815$, and $R_{\text{test}} = 0.8782$, indicating good generalization with limited over-

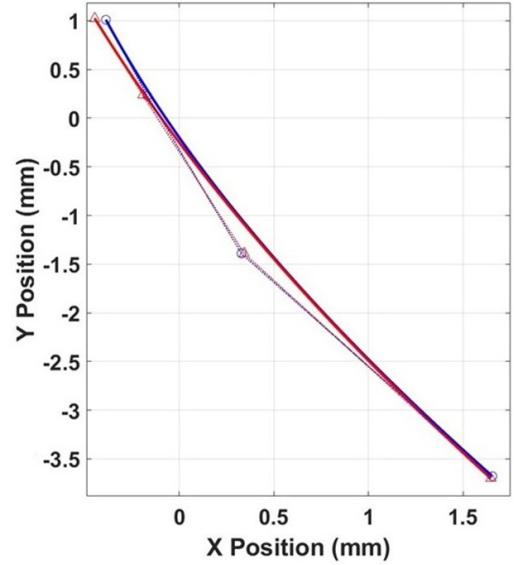


Figure 12: Bezier curve shape prediction (side view). Ground truth (blue) vs. RF predictions (green).

Table 3: Comparison of learning models on the test set.

Model	Error metrics				Timing	
	RMSE (mm)	R ²	Mean $\sum e^2$	SD $\sum e^2$	Train (s)	Pred / sample (s)
NN	0.121	0.788	0.283	0.329	176.2	1.07×10^{-4}
RF	0.0868	0.816	0.131	0.204	26.9	7.89×10^{-5}

fitting. Nevertheless, the RF model surpassed the NN across every metric. Using the test set, we formed per-sample total errors $\sum_{i=1}^{12} (y_i - \hat{y}_i)^2$ for both models. Lilliefors tests detected slight departures from perfect normality for NN and RF residuals ($p = 0.001$ for each). Levene's test showed unequal variances ($p = 4.96 \times 10^{-21}$); consequently, Welch's two-sample t -test was applied, revealing a highly significant reduction in error for RF compared with NN ($t = 12.55$, $p = 1.32 \times 10^{-34}$). Mean (\pm SD) total error fell from 0.283 ± 0.329 for the NN to 0.131 ± 0.204 for the RF (Table 3). These findings confirm that model selection materially influences residual error and reinforce our choice of RF for subsequent real-time deployment.

4.5. FBG Ground Truth Limitations and Accuracy

The accuracy validation methodology of this study warrants careful examination, particularly regarding the use of reconstructed shapes from FBG as ground truth for training the learning based models. While multi-core fiber Bragg grating sensors are well-established for shape sensing in medical robotics applications, their inherent limitations must be acknowledged when interpreting the reported accuracy metrics. The FBG system employed in this study is notably coarser than comparable studies, such as Dong et al. [33], who achieved 3.17 mm grating spacing and validated their FBG measurements against electromagnetic tracking, reporting 1.53 mm tip position accuracy. The piecewise constant curvature assumption between grating points introduces interpolation errors that accumulate along the

fiber length, potentially resulting in tip position uncertainties exceeding 1 mm despite the sensor's high strain sensitivity.

The reported sub-millimeter accuracy (0.064 mm RMSE) in this work specifically quantifies the Random Forest model's ability to predict Bezier control points that, when used to reconstruct the shape, closely match the FBG-derived measurements. This metric should not be interpreted as absolute shape sensing accuracy, but rather as the model's capacity to learn and reproduce the mapping between magnetic field inputs and FBG-measured deformations. The distinction is critical: while the learning-based approach successfully captures the nonlinear relationship between actuation and measured response with high fidelity, the absolute accuracy of the predicted shapes relative to true physical deformation remains bounded by the FBG system's inherent limitations. Future work should incorporate independent validation using calibrated vision systems or higher resolution tracking methods to establish absolute accuracy bounds. Despite these limitations, the learning-based approach remains valid for the intended application of closed-loop control, where consistent relative shape prediction is more critical than absolute position accuracy. The model's ability to predict deformation patterns with high repeatability enables effective navigation control even if absolute position uncertainty exists, as the controller can compensate for systematic errors through feedback mechanisms.

Furthermore, this study utilized only a single physical prototype with data collected across 70 actuation scenarios, preventing assessment of device-to-device variability or manufacturing tolerances. The learning-based model is inherently device-specific, trained on this particular prototype's characteristics without validation across multiple devices. Clinical translation would necessitate either individual calibration for each manufactured device or training across multiple prototypes to establish model robustness. While the current work demonstrates the feasibility of the learning-based approach for shape prediction, comprehensive validation across multiple devices with varying material properties and manufacturing variations remains essential for establishing clinical applicability and generalization capabilities of the proposed methodology.

Lastly, the current study trained and evaluated the model exclusively using uniform, symmetric rotating magnetic fields generated under controlled laboratory conditions. Clinical environments present significantly more complex magnetic field profiles, including spatial non-uniformities, field gradients, and asymmetric distributions caused by nearby ferromagnetic materials, imaging equipment, or electromagnetic interference. The learning-based model's performance under such irregular field conditions remains untested and would likely degrade without prior exposure to these variations during training. Robust clinical deployment would require expanding the training dataset to encompass diverse magnetic field profiles representative of surgical environments, including both measured clinical field distributions and systematically varied asymmetric patterns. This expanded training approach would enable the model to learn invariant features across field variations rather than overfitting to idealized uniform fields.

5. CONCLUSION

This paper presented the first learning-based approach that transforms FBG shape sensing data into Bezier control points for modeling magnetically actuated soft surgical instruments. This novel approach bridges the gap between shape sensing technologies and practical control applications by providing a direct mapping between the magnetic field and the resulting device configuration. Our key contribution was the development and validation of a framework that enables highly accurate real-time shape prediction of complex non-linear deformations in soft robotic devices. By comparing NN and RF modeling approaches, we demonstrated that ensemble-based methods outperform traditional NN for this application, particularly at the critical distal end of the device, where precise control is essential for surgical tasks. Also, the computational efficiency of our approach supports high-frequency real-time control suitable for dynamic surgical environments, while maintaining sub-millimeter accuracy across the device's entire structure. Future work will focus on three main directions: (1) integrating this modeling approach into a closed-loop control system for autonomous navigation, (2) expanding the training dataset to include additional device configurations for enhanced generalization, and (3) validating the model through ex vivo experiments in simulated surgical scenarios.

Funding Source Statement

This work was supported by the Canadian Institutes of Health Research (CIHR) Project Grant 452287.

Declaration of Competing Interest

The authors declare that they have no competing financial interests or personal relationships that could have influenced the work reported in this paper.

Declaration of Generative AI Use

The author(s) used ChatGPT for grammar and language checking only. No scientific content was generated using AI. The author(s) reviewed and edited the content and take full responsibility for the published article.

Data Availability

Data will be made available on request.

References

- [1] R. Martinez-Perez, L. C. Requena, R. L. Carrau, D. M. Prevedello, Modern endoscopic skull base neurosurgery, *Journal of neuro-oncology* 151 (2021) 461–475.

- [2] P. Gholami, K. Rezvanfar, S. Valizadehashenaabad, E. Esmaeili, F. Rafizadeh, A. Aminiyan, M. S. Fakhr, *Advances and challenges in endoscopic endonasal tumor surgery: Lessons learned from modern practice*, *Indian Journal of Otolaryngology and Head & Neck Surgery* (2025) 1–22.
- [3] Y. Sasagawa, S. Tanaka, M. Kinoshita, M. Nakada, *Endoscopic and exoscopic surgery for brain tumors*, *International Journal of Clinical Oncology* 29 (10) (2024) 1399–1406.
- [4] Y. H. Kim, J. Y. Lee, J. H. Phi, K.-C. Wang, S.-K. Kim, *Endoscopic endonasal skull base surgery for pediatric brain tumors*, *Child’s Nervous System* 35 (2019) 2081–2090.
- [5] B. A. Valencia-Sanchez, J. D. Kim, S. Zhou, S. Chen, M. L. Levy, C. Roxbury, V. A. Patel, S. P. Polster, *Special considerations in pediatric endoscopic skull base surgery*, *Journal of Clinical Medicine* 13 (7) (2024) 1924.
- [6] M. Roshanfar, A. Sayadi, J. Dargahi, A. Hooshlar, *Stiffness adaptation of a hybrid soft surgical robot for improved safety in interventional surgery*, in: *2022 44th Annual International Conference of the IEEE Engineering in Medicine & Biology Society (EMBC)*, IEEE, 2022, pp. 4853–4859.
- [7] J. Burgner, D. C. Rucker, H. B. Gilbert, P. J. Swaney, P. T. Russell, K. D. Weaver, R. J. Webster, *A telerobotic system for transnasal surgery*, *IEEE/ASME transactions on mechatronics* 19 (3) (2013) 996–1006.
- [8] M. F. Rox, D. S. Ropella, R. J. Hendrick, E. Blum, R. P. Naftel, H. C. Bow, S. D. Herrell, K. D. Weaver, L. B. Chambless, R. J. Webster III, *Mechatronic design of a two-arm concentric tube robot system for rigid neuroendoscopy*, *IEEE/ASME transactions on mechatronics* 25 (3) (2020) 1432–1443.
- [9] Z. Yang, H. Yang, Y. Cao, Y. Cui, L. Zhang, *Magnetically actuated continuum medical robots: A review*, *Advanced intelligent systems* 5 (6) (2023) 2200416.
- [10] M. Roshanfar, M. Salimi, A. H. Kaboodrangi, S.-J. Jang, A. J. Sinusas, S.-C. Wong, B. Mosadegh, *Advanced robotics for the next-generation of cardiac interventions*, *Micromachines* 16 (4) (2025) 363.
- [11] M. Roshanfar, C. He, L. Huang, Z. Li, L. Cheng, D. J. Podolsky, T. Looi, E. Diller, *3-dof magnetically actuated robotic manipulator for precision soft tissue resection*, in: *2025 International Conference on Manipulation, Automation and Robotics at Small Scales (MARSS)*, IEEE, 2025, pp. 1–6.
- [12] J. J. Abbott, E. Diller, A. J. Petruska, *Magnetic methods in robotics*, *Annual Review of Control, Robotics, and Autonomous Systems* 3 (1) (2020) 57–90.
- [13] C. He, R. Nguyen, H. Mayer, L. Cheng, P. Kang, D. A. Aubeeluck, G. Thiong’o, E. Fredin, J. Drake, T. Looi, et al., *Magnetically actuated dexterous tools for minimally invasive operation inside the brain*, *Science Robotics* 10 (100) (2025) eadh4249.
- [14] R. Dreyfus, Q. Boehler, S. Lyttle, P. Gruber, J. Lussi, C. Chautems, S. Gervasoni, J. Berberat, D. Seibold, N. Ochsenbein-Kölble, et al., *Dexterous helical magnetic robot for improved endovascular access*, *Science Robotics* 9 (87) (2024) eadh0298.
- [15] Y. Deng, M. Roshanfar, H. Mayer, C. He, J. Drake, T. Looi, E. Diller, *Towards bimanual operation of magnetically actuated surgical instruments*, in: *2024 10th IEEE RAS/EMBS International Conference for Biomedical Robotics and Biomechatronics (BioRob)*, IEEE, 2024, pp. 1295–1300.
- [16] G. Pittiglio, P. Lloyd, T. da Veiga, O. Onaizah, C. Pompili, J. H. Chandler, P. Valdastrì, *Patient-specific magnetic catheters for atraumatic autonomous endoscopy*, *Soft robotics* 9 (6) (2022) 1120–1133.
- [17] W. Chen, J. Sui, C. Wang, *Magnetically actuated capsule robots: A review*, *IEEE Access* 10 (2022) 88398–88420.
- [18] T. Lee, E. Diller, *Magnetic capsule for stable collection of large gi tract microbiome samples*, in: *2025 International Conference on Manipulation, Automation and Robotics at Small Scales (MARSS)*, IEEE, 2025, pp. 1–7.
- [19] C. Chautems, S. Lyttle, Q. Boehler, B. J. Nelson, *Design and evaluation of a steerable magnetic sheath for cardiac ablations*, *IEEE Robotics and Automation Letters* 3 (3) (2018) 2123–2128. doi:10.1109/LRA.2018.2809546.
- [20] Y. Kim, G. A. Parada, S. Liu, X. Zhao, *Ferromagnetic soft continuum robots*, *Science Robotics* 4 (33) (2019) eaax7329.
- [21] N. Li, D. Lin, J. Wu, Q. Gan, N. Jiao, *Dexterity of concentric magnetic continuum robot with multiple stiffness*, in: *International Conference on Intelligent Robotics and Applications*, Springer, 2023, pp. 329–338.
- [22] A. Hong, A. J. Petruska, A. Zemmar, B. J. Nelson, *Magnetic control of a flexible needle in neurosurgery*, *IEEE Transactions on Biomedical Engineering* 68 (2) (2020) 616–627.
- [23] M. Roshanfar, A. Zhang, C. He, A. Hooshlar, J. Drake, T. Looi, E. Diller, *Soft magnetically steerable suction device for endoscopic endonasal brain tumor extraction*, in: *2025 IEEE 8th International Conference on Soft Robotics (RoboSoft)*, IEEE, 2025, pp. 1–6.
- [24] M. Roshanfar, S. Taki, A. Sayadi, R. Cecere, J. Dargahi, A. Hooshlar, *Hyperelastic modeling and validation of hybrid-actuated soft robot with pressure-stiffening*, *Micromachines* 14 (5) (2023) 900.

- [25] N. Masoumi, A. C. Ramos, T. Torkaman, L. S. Feldman, J. Barralet, J. Dargahi, A. Hooshlar, Embedded force sensor for soft robots with deep transformation calibration, *IEEE Transactions on Medical Robotics and Bionics* (2024).
- [26] T. Torkaman, M. Roshanfar, J. Dargahi, A. Hooshlar, Embedded six-dof force–torque sensor for soft robots with learning-based calibration, *IEEE Sensors Journal* 23 (4) (2023) 4204–4215.
- [27] A. Hooshlar, A. Sayadi, M. Jolaei, J. Dargahi, Accurate estimation of tip force on tendon-driven catheters using inverse cosserat rod model, in: *2020 International Conference on Biomedical Innovations and Applications (BIA)*, IEEE, 2020, pp. 37–40.
- [28] M. Jolaei, A. Hooshlar, A. Sayadi, J. Dargahi, M. Packirisamy, Sensor-free force control of tendon-driven ablation catheters through position control and contact modeling, in: *2020 42nd annual international conference of the IEEE engineering in medicine & biology society (EMBC)*, IEEE, 2020, pp. 5248–5251.
- [29] A. Sayadi, R. Cecere, A. Hooshlar, Finite arc method: fast-solution extended piecewise constant curvature model of soft robots with large variable curvature deformations, *Robotics Reports* 2 (1) (2024) 49–64.
- [30] O. Al-Ahmad, M. Ourak, J. Vlekken, E. Vander Poorten, Fbg-based estimation of external forces along flexible instrument bodies, *Frontiers in Robotics and AI* 8 (2021) 718033.
- [31] Carbon, Inc., SIL 30 Technical Datasheet, doc #106453-00 Rev F (2024).
URL <https://www.carbon3d.com/materials/sil-30>
- [32] A. Schonewille, C. He, C. Forbrigger, N. Wu, J. Drake, T. Looi, E. Diller, Electromagnets under the table: an unobtrusive magnetic navigation system for microsurgery, *IEEE Transactions on Medical Robotics and Bionics* 6 (3) (2024) 980–991.
- [33] Z. Dong, X. Wang, G. Fang, Z. He, J. D.-L. Ho, C.-L. Cheung, W. L. Tang, X. Xie, L. Liang, H.-C. Chang, et al., Shape tracking and feedback control of cardiac catheter using mri-guided robotic platform—validation with pulmonary vein isolation simulator in mri, *IEEE Transactions on Robotics* 38 (5) (2022) 2781–2798.